

Coexistence of cluster structure and superdeformation in ^{44}Ti studied with deformed-basis antisymmetrized molecular dynamics

Masaaki KIMURA¹ and Hisashi HORIUCHI²

¹*RI-beam Science Laboratory, RIKEN (The Institute of Physical and
Chemical Research), Wako, Saitama 351-0198, Japan.*

²*Department of Physics, Kyoto University, Kitashirakawa, Kyoto 606-8502,
Japan*

Abstract

The nucleus ^{44}Ti has low-lying levels of various kinds of mutually very different nuclear structure displaying the richness of the nuclear many-body dynamics. It is shown that the deformed-basis antisymmetrized molecular dynamics by the use of the Gogny D1S force reproduces successfully and unifiedly two types of coexistence phenomena in ^{44}Ti . Namely, on one hand, the coexistence of the mean field structure and the cluster structure is confirmed by verifying the normally deformed structure of the $K^\pi=3_1^-$ band with a 1-particle-jump intrinsic configuration and the $\alpha+^{40}\text{Ca}$ cluster structure of the $K^\pi=0_2^-$ band. The mixed character of the mean-field-like structure and the $\alpha+^{40}\text{Ca}$ cluster structure of the ground band is also shown. On the other hand, the coexistence of the normal deformed mean field and the superdeformed mean field is confirmed by verifying the triaxial superdeformation of the $K^\pi=0_2^+$ band and the $K^\pi=2_1^+$ band which has a 4-particle-jump intrinsic configuration. Good reproduction of the experimental data is shown for many kinds of quantities including the energy spectra, electric transition rates, alpha spectroscopic factors. Preliminary discussions are given on the existence of hyperdeformed excited states, the relation between superdeformation and clustering and so on.

§1. Introduction

The nucleus ^{44}Ti is the lightest $N=Z$ even-even nucleus in the pf shell region and its structure is very important for the study of the neutron-proton correlation in the pf shell region. Since we can now expect the increasing experimental information about the proton-rich nuclei along the $N\sim Z$ line up to $A\sim 100$, the study of the neutron-proton correlation in ^{44}Ti is even more important than before. ^{44}Ti is analogous to ^{20}Ne in the sense that both nuclei have two neutrons and two protons outside the doubly closed-shell core nuclei ^{40}Ca and ^{16}O , respectively. It is well known^{1),2)} that ^{20}Ne has non-small α -clustering character even in the ground band states and much prominent $\alpha+^{16}\text{O}$ cluster structure in some of its excited bands. Therefore there have been many microscopic theoretical works to investigate possible α -cluster structure in ^{44}Ti .^{3),4)} However, more convincing argument⁵⁾ than these microscopic studies about the α -clustering in ^{44}Ti was obtained from the knowledge of the so-called unique α - ^{40}Ca optical potential which was established by the study of the elastic α - ^{40}Ca scattering including ALAS (anomalous large angle scattering) and nuclear rainbow phenomena.⁶⁾ From the fact that the band head 0^+ state of the lowest rotational band of this unique α - ^{40}Ca optical potential is located several MeV below the α - ^{40}Ca threshold, the lowest band was assigned to correspond to the ground rotational band of ^{44}Ti ,⁵⁾ which means that the ground band states of ^{44}Ti should have sizable amount of component of $\alpha+^{40}\text{Ca}$ cluster structure. Furthermore, the $K^\pi=0^-$ band which is the parity-doublet partner of the lowest band ($K^\pi=0^+$) was predicted to exist with its band head 1^- state a few MeV higher above the $\alpha+^{40}\text{Ca}$ threshold. A similar argument was also presented by a microscopic approach⁷⁾ which fitted α - ^{40}Ca scattering data in addition to the usual structure study of the bound states of ^{44}Ti . The parity-doublet partner band with $K^\pi=0^-$ was actually found later experimentally by using α -transfer reaction.⁸⁾

It is usually considered that the formation of the mean field becomes much more firm in the pf shell and heavier mass region compared with the smaller mass region where the α clustering is active especially below the mass $A\sim 30$. However, recent experiments show that the mean field around the mass $A\sim 40$ is not simply static but dynamic in its nature. It is because recently many low-lying rotational spectra associated with superdeformed bands have been observed in rather light mass regions including the mass $A\sim 40$ region.^{9)–11)} In the case of ^{44}Ti , the rotational band built upon the excited 0_2^+ state at 1.905 MeV¹²⁾ was found to extend up to the $J^\pi=12^+$ state and was discussed to have superdeformed structure.¹¹⁾ According to the shell model and mean-field-type calculations of ^{44}Ti ,^{11),13)–15)} this superdeformed structure is regarded as having a 4-particle-jump configuration, namely 8p-4h configuration. The appearance of the superdeformed mean field in a very low excitation

energy region indicates the presence of the active dynamics of the mean-field formation.

As is shown in the above discussions, ^{44}Ti is a typical nucleus which displays to us vividly the richness and profoundness of the nuclear many-body dynamics. Namely in ^{44}Ti we have the coexistence of the α -clustering dynamics and the mean-field dynamics, and also the coexistence of the normal deformed mean field and superdeformed mean field. Therefore it is an important and challenging task for the nuclear theory to describe properly and unifiedly these two kinds of coexistence phenomena of the nuclear structure dynamics displayed in ^{44}Ti . We think that the proper description of these two kinds of coexistence phenomena in ^{44}Ti is indispensable for us in order to get the proper understanding of the neutron-proton correlation in the pf -shell region and also in the proton-rich region along $N \approx Z$ line. In our recent study of ^{32}S ,^{16),17)} we have concluded that the superdeformed excited band which is predicted by many mean-field calculations¹⁸⁾⁻²⁰⁾ to exist with its band-head 0^+ state around 9 MeV above the ground state can be regarded also as being an $^{16}\text{O} + ^{16}\text{O}$ molecular band which is predicted to exist in the same excitation energy region from the ^{16}O - ^{16}O unique optical potential studies.^{21),22)} This result of ours about ^{32}S demands us that we should study also in ^{44}Ti the interplay and the relation between the cluster structure and the superdeformed mean-field structure.

The purpose of this paper is to study the above-mentioned two kinds of coexistence phenomena in ^{44}Ti by using a single theoretical framework of the deformed-basis AMD (antisymmetrized molecular dynamics).^{2),17),23)} The deformed-basis AMD is very suited for our present study because the AMD method is a kind of *ab initio* theory which enables us to study the clustering dynamics without assuming the existence of any clusters,¹⁷⁾ and also because, by the use of the deformed basis, the AMD can describe even the superdeformed mean field yielding almost the same quantitative results as the mean field theory. We will report that the AMD calculation by the use of the Gogny D1S force²⁴⁾ surely reproduces and hence confirms the existence of the two kinds of coexistence in ^{44}Ti . Namely, firstly as for the confirmation of the coexistence of the α -clustering dynamics and the mean-field dynamics, we have obtained the $K^\pi=0^-$ band with prominent $\alpha+^{40}\text{Ca}$ structure and the $K^\pi=3^-$ band with prominent mean-field-like structure having a 1-particle-jump dominant configuration. Furthermore we have found the mixture of the $\alpha+^{40}\text{Ca}$ clustering character and the mean-field character in the $K^\pi=0^+$ ground band states. In the case of the ground state, the calculated $\alpha+^{40}\text{Ca}$ component is about 40%. When we judge from the usual expectation that in ^{44}Ti the mean field is formed more firmly than in ^{20}Ne and also the spatial-symmetry-breaking (hence α -cluster-breaking) spin-orbit force has stronger effects than in ^{20}Ne , it seems that we may doubt the α -clustering character in the ground band. However, the above-mentioned result of our calculation gives us an important theoretical

confirmation of the non-small $\alpha+^{40}\text{Ca}$ clustering character of the ground band, which is consistent with the study by the use of the unique $\alpha\text{-}^{40}\text{Ca}$ optical potential mentioned before. Just like we have obtained the $K^\pi=3^-$ band which is formed by the excitation of the single-particle degree of freedom from the mean-field-structure component contained in the ground band, we have obtained, on the other hand, an excited band which is formed by the excitation of the inter-cluster relative motion from the $\alpha+^{40}\text{Ca}$ -structure component contained in the ground band. This excited band with $K^\pi=0^+$ has been already reported to be observed experimentally and our AMD results are consistent to this experimental report. Secondly, as for the confirmation of the coexistence of the normal deformed mean field and superdeformed mean field, we have obtained, in addition to the normal deformation of the ground band and the $K^\pi=3^-$ band, the superdeformation of the $K^\pi=0_2^+$ band upon the 0_2^+ state which has 4-particle-jump intrinsic configuration with large deformation parameter $\beta\sim 0.5$ and with large γ parameter $\gamma\sim 25^\circ$. Due to this triaxiality of the superdeformation we have also obtained a $K^\pi=2_1^+$ superdeformed side band which we consider to correspond to the observed $K^\pi=2_1^+$ band upon the 2_3^+ state at 2.88 MeV. The triaxiality of the ^{44}Ti superdeformation was also reported in Ref.¹⁵⁾

The contents of this paper are as follows: In the next section (section 2), we briefly explain the formalism of the deformed-basis AMD and the generator coordinate calculation in which the constrained deformed-basis AMD wave functions are superposed after the angular momentum projection. In section 3, we discuss the energy surfaces with good spins as functions of the deformation parameter β and the comparison of calculated energy spectra with experiments. The density distributions of the obtained intrinsic wave functions are discussed. The existence of the highly excited states with hyperdeformed structure is also suggested. In section 4, we discuss the obtained level scheme of ^{44}Ti which includes many kinds of the nuclear structure. Firstly, we explain the existence of the different kinds of the nuclear excitations in this nucleus together with making the comparison with the available experimental data such as the excitation energies and the $E2$ transition probabilities. Then we focus on the $\alpha+^{40}\text{Ca}$ clustering in the obtained level scheme. The $\alpha+^{40}\text{Ca}$ component in the ground band is analyzed and the excitations of the inter-cluster motion in the excited bands are discussed. Section 5 is for summarizing discussions.

§2. Framework of the deformed-basis antisymmetrized molecular dynamics plus generator coordinate method

In this section, the framework of the deformed-basis AMD+GCM is explained briefly. For more detailed explanation of the framework of the deformed-basis AMD, readers are

referred to references.^{2),17)} The intrinsic wave function of the system with mass A is given by a Slater determinant of single-particle wave packets $\varphi_i(\mathbf{r})$;

$$\Phi_{int} = \frac{1}{\sqrt{A!}} \det\{\varphi_1, \varphi_2, \dots, \varphi_A\}, \quad (2.1)$$

$$\varphi_i(\mathbf{r}) = \phi_i(\mathbf{r})\chi_i\xi_i, \quad (2.2)$$

where the single-particle wave packet φ_i consists of the spatial ϕ_i , spin χ_i and isospin ξ_i parts. Deformed-basis AMD employs the triaxially deformed Gaussian centered at \mathbf{Z}_i as the spatial part of the single-particle wave packet.

$$\begin{aligned} \phi_i(\mathbf{r}) &\propto \exp\left\{-\sum_{\sigma=x,y,z} \nu_\sigma (r_\sigma - Z_{i\sigma})^2\right\}, \\ \chi_i &= \alpha_i\chi_\uparrow + \beta_i\chi_\downarrow, \quad |\alpha_i|^2 + |\beta_i|^2 = 1 \\ \xi_i &= \textit{proton} \quad \text{or} \quad \textit{neutron}. \end{aligned} \quad (2.3)$$

Here, the complex number parameter \mathbf{Z}_i which represents the centroid of the Gaussian in the phase space takes independent value for each nucleon. The width parameters ν_x, ν_y and ν_z are real number parameters and take independent values for x, y and z directions, but are common to all nucleons. Spin part χ_i is parametrized by α_i and β_i and isospin part ξ_i is fixed to up (proton) or down (neutron). $\mathbf{Z}_i, \nu_x, \nu_y, \nu_z$ and α_i, β_i are the variational parameters and optimized by the method of frictional cooling. The advantage of the triaxially deformable single-particle wave packet is that it makes possible to describe the cluster-like structure and deformed mean-field structure within a single framework which is discussed in detail in reference.²⁾

As the variational wave function, we employ the parity projected wave function as in the same way as many other AMD studies

$$\Phi^\pm = P^\pm \Phi_{int} = \frac{(1 \pm P_x)}{2} \Phi_{int}, \quad (2.4)$$

here P_x is the parity operator and Φ_{int} is the intrinsic wave function given in Eq(2.1). Parity projection makes possible to determine the different structure of the intrinsic state for the different parity states.

Hamiltonian used in this study is as follows;

$$\hat{H} = \hat{T} + \hat{V}_n + \hat{V}_c - \hat{T}_g, \quad (2.5)$$

where \hat{T} and \hat{T}_g are the total kinetic energy and the energy of the center of mass motion, respectively. We have used the Gogny force with D1S parameter set as an effective nuclear

force \hat{V}_n . Coulomb force \hat{V}_c is approximated by the sum of seven Gaussians. The energy variation is made under the constraint on the nuclear quadrupole deformation by adding to \hat{H} a constraint potential $V_{cst} = v_{cst}(\langle\beta\rangle^2 - \beta_0^2)^2$ with a large positive value for v_{cst} . At the end of the variational calculation, the expectation value of V_{cst} should be zero in principle and in the practical calculation, we confirm it is less than 0.1keV. The optimized wave function is denoted by $\Phi^\pm(\beta_0)$. Here it should be noted that this constraint does not refer to the deformation parameter γ , which means that $\Phi^\pm(\beta_0)$ with positive β_0 can be not only prolate but also oblate.

From the optimized wave function, we project out the eigenstate of the total angular momentum J ,

$$\Phi_{MK}^{J\pm}(\beta_0) = P_{MK}^J \Phi^\pm(\beta_0) = P_{MK}^J P^\pm \Phi_{int}(\beta_0). \quad (2.6)$$

Here P_{MK}^J is the total angular momentum projector. The integrals over the three Euler angles included in the P_{MK}^J are evaluated by the numerical integration.

Furthermore, we superpose the wave functions $\Phi_{MK}^{J\pm}$ which have the same parity and the angular momentum but have different value of deformation parameter β_0 and K . Thus the final wave function of the system becomes as follows;

$$\Phi_n^{J\pm} = c_n \Phi_{MK}^{J\pm}(\beta_0) + c'_n \Phi_{MK'}^{J\pm}(\beta'_0) + \dots, \quad (2.7)$$

where other quantum numbers except total angular momentum and parity are represented by n . The coefficients c_n, c'_n, \dots are determined by the Hill-Wheeler equation,

$$\delta(\langle\Phi_n^{J\pm}|\hat{H}|\Phi_n^{J\pm}\rangle - E_n\langle\Phi_n^{J\pm}|\Phi_n^{J\pm}\rangle) = 0. \quad (2.8)$$

In order to analyze the obtained wave function $\Phi_{MK}^{J\pm}(\beta_0)$, we extract the single particle structure of $\Phi_{int}(\beta_0)$ by constructing the Hartree-Fock Hamiltonian from $\Phi_{int}(\beta_0)$ as follows.²⁵⁾ When the optimized wave function $\Phi_{int}^\pm(\beta_0) = P^\pm \frac{1}{\sqrt{A!}} \det\{\varphi_1, \varphi_2, \dots, \varphi_A\}$ is given, we calculate the orthonormalized basis ϕ_α which is a linear combination of the single-particle wave packets φ_i ,

$$\phi_\alpha = \frac{1}{\sqrt{\mu_\alpha}} \sum_{i=1}^A c_{i\alpha} \varphi_i. \quad (2.9)$$

Here, μ_α and $c_{i\alpha}$ are the eigenvalue and eigenvector of the overlap matrix $B_{ij} \equiv \langle\varphi_i|\varphi_j\rangle$,

$$\sum_{j=1}^A B_{ij} c_{j\alpha} = \mu_\alpha c_{i\alpha}, \quad (2.10)$$

and it is clear that $\{\phi_\alpha\}$ are orthonormalized from this relation. Using this basis set of ϕ_α , we calculate the Hartree-Fock single-particle Hamiltonian $h_{\alpha\beta}$ which is defined as,

$$h_{\alpha\beta} \equiv \langle \phi_\alpha | \hat{t} | \phi_\beta \rangle + \sum_{\gamma=1}^A \langle \phi_\alpha \phi_\gamma | \hat{v} | \widetilde{\phi_\beta \phi_\gamma} \rangle + \frac{1}{2} \sum_{\gamma\delta} \langle \phi_\gamma \phi_\delta | \phi_\alpha^* \phi_\beta \frac{\partial \hat{v}}{\partial \rho} | \widetilde{\phi_\gamma \phi_\delta} \rangle. \quad (2.11)$$

By the diagonalization of $h_{\alpha\beta}$, we obtain the single-particle energy ϵ_s and single-particle wave function $\tilde{\phi}_s$.

$$\sum_{\beta=1}^A h_{\alpha\beta} f_{\beta s} = \epsilon_s f_{\alpha s}, \quad (2.12)$$

$$\tilde{\phi}_s = \sum_{\alpha=1}^A f_{\alpha s} \phi_\alpha. \quad (2.13)$$

We note that the single-particle energy ϵ_s and wave function $\tilde{\phi}_s$ are obtained for occupied states but not for unoccupied states from this method. Furthermore, since the actual variational calculation is made after the parity projection (the superposition of the two Slater determinants), it does not allow the naive interpretation of $\phi^\pm(\beta_0)$ by the single-particle picture. However, the single-particle structure obtained by this method is useful to estimate the particle-hole structure of the obtained wave function. From the parity $\pi_s^\pm = \langle \tilde{\phi}_s | P^\pm | \tilde{\phi}_s \rangle$ and the the angular momentum $\langle \tilde{\phi}_s | \hat{l}^2 | \tilde{\phi}_s \rangle$, we have estimated the particle-hole structure which is denoted as ‘ $n\hbar\omega$ structure’ in the following.

§3. Energy curves of the positive- and negative- parity states

3.1. Positive parity states

After the variation and angular momentum projection, we obtain the energy curves as functions of the matter quadrupole deformation parameter β . Before discussing the low-lying states of ^{44}Ti , we study the features of the energy curves to clarify the characters of the wave functions on the energy curves. The positive-parity energy curve (figure 1) has three energy minima in each spin state and the wave functions at these minima have different particle-hole configurations. The wave functions around the minimum at $\beta=0.2$ have the $0\hbar\omega$ configuration and they contribute to the ground band. Each spin state has a parity symmetric intrinsic density distribution and does not show the apparent existence of an $\alpha+^{40}\text{Ca}$ cluster correlation. The centroids of the single particle wave packets are gathered around the center of the nucleus, that is in contrast to the case of the ^{20}Ne ground band

in which single particle wave packets are separated into two parts (4+16) describing the spatially separated α and ^{16}O subunits. But as we will discuss in the next section, each spin states (except 10^+ and 12^+) around $\beta=0.20$ contains $\alpha+^{40}\text{Ca}$ cluster correlation. Around $\beta=0.35$, the change of the single particle configuration occurs and the wave function has a $4\hbar\omega$ configuration in which four nucleons are excited into the pf -shell from ^{40}Ca core. This type of the configuration has its energy minimum around $\beta=0.5$. Interestingly, the excitation energy of this $4\hbar\omega$ state with respect to the $0\hbar\omega$ state is quite small after the angular momentum projection. In the present result, it is only 1.7MeV in the case of the 0^+ state. The angular momentum projection lowers the energy of this state by about 6MeV. This state corresponds to the band head state of the superdeformed $K^\pi=0_2^+$ band which starts from the 0_2^+ state at 1.9 MeV in experiments. Furthermore, this state has a triaxially deformed intrinsic density distribution ($\gamma=0.25$) as is shown in figure 2. The triaxial deformation of this state have been also pointed out by the Hartree-Fock calculation¹⁵⁾ which is also free from any assumptions on the deformation symmetry of wave function. When we perform angular momentum projection, this triaxial deformation produces the $K^\pi=2^+$ band together with the $K^\pi=0_2^+$ band mentioned above. In figure 1, only the 2^+ state is plotted among the $K^\pi=2^+$ band members to avoid the unsightliness of this figure. At larger deformation, the energy of the system increases rapidly, but again it has third local minimum around $\beta=0.7$. Its energy is higher by about 19MeV than the $0\hbar\omega$ state in the case of 0^+ state. Though the quadrupole deformation is not large enough, this state can be regarded as the hyperdeformed state, if we regarded the $4\hbar\omega$ state around $\beta=0.5$ as the superdeformed state. Because of the large parity asymmetry of the wave function, the system has the parity mixed single particle orbits and it makes hard to define the particle-hole structure of the usual single particle picture. It is notable that the density distribution of this state shows the possible relationship with the $^{16}\text{O}+^{28}\text{Si}$ molecular structure. Different from other states, the centroids of the single particle wave packets are separated into two parts (16 packets at left side and 28 packets at right side in figure 2 (e)) describing spatially separated ^{16}O and ^{28}Si .

3.2. *Negative parity states*

Next, we discuss the negative-parity energy curves (figure 3) whose behavior is rather complicated than that of the positive-parity states. In the negative-parity states of this nucleus, the intrinsic wave functions have parity mixed single particle orbits. Therefore, we cannot conclude the definite $\hbar\omega$ structure, though for the presentation we denote these structure with the $\hbar\omega$ notation which is roughly estimated from the parity of the single particle orbit. In the small deformation region, we obtained the $K^\pi=3^-$ and $K^\pi=0^-$ bands and both have minima around $\beta=0.25$. Roughly speaking, the intrinsic wave functions of

these states have $1\hbar\omega$ structure. The $K^\pi=3^-$ band corresponds to the observed lowest negative-parity $K^\pi=3^-$ band, while the existence of the $K^\pi=0^-$ band in this energy region has not been established in experiments. In the medium deformed region around $\beta=0.4$, we have obtained other $K^\pi=0^-$ and $K^\pi=3^-$ bands which are also not established in experiments. In these bands, $3\hbar\omega$ and $5\hbar\omega$ structures are mixed and they can be regarded as the $1\hbar\omega$ de-excited and excited states of the triaxial superdeformed state with the positive-parity, although their triaxiality are smaller than that of the positive-parity states. Their triaxial deformation are about $\gamma=0.16^\circ$ at most.

Interestingly, we have also found the local minimum between the $1\hbar\omega$ structure and $3\hbar\omega$ ($5\hbar\omega$) structure which is located around $\beta=0.27$. This intrinsic state is obtained by performing the frictional cooling calculation using the $\alpha+^{40}\text{Ca}$ Brink wave function as the initial wave function. In this calculation, this structure continues to be stable during the cooling variational calculation after the parity projection to the negative-parity, although of course, the wave function considerably deviates from the initial Brink wave function through the cooling. It is contrasting to the case of the positive-parity state, in which the α particle is absorbed into the ^{40}Ca core even when we start the cooling from the $\alpha+^{40}\text{Ca}$ Brink wave function. This state corresponds to the theoretically suggested^{5),7)} and experimentally observed⁸⁾ $\alpha+^{40}\text{Ca}$ cluster structure with the negative-parity. However, we will see in the next section that this band is strongly mixed with the above mentioned $K^\pi=0^-$ band ($3\hbar\omega$ and $5\hbar\omega$) after the GCM calculation and this mixing causes the fragmentation of the $\alpha+^{40}\text{Ca}$ rotational band states with negative-parity. In the largely deformed region, we found the counter part which originates from the parity asymmetry of the $^{16}\text{O}+^{28}\text{Si}$ structure obtained in the positive-parity state. The $^{16}\text{O}+^{28}\text{Si}$ structure with the negative parity gives rise to a $K^\pi=0^-$ band.

§4. Variety of the nuclear structure in the low-lying states of ^{44}Ti

The calculated and observed level schemes of ^{44}Ti are presented in figure 5. In this section, we discuss the obtained level schemes together with other calculated quantities such as the $E2$ transition probabilities. Firstly, we discuss the different characteristics of the ground and excited states. Then we focus on the $\alpha+^{40}\text{Ca}$ clustering in this nucleus. We will see that the observed eight rotational bands shown in figure 5 are all reproduced well by the theory.

4.1. Low-lying level scheme

4.1.1. $K^\pi=0_1^+$ ground band

The ground band member states mainly consist of the $0\hbar\omega$ structure and are obtained up to the 12^+ state. The obtained binding energy of the ground state is -372.4MeV which underestimates the observed value by 3 MeV. The excitation energies of the ground band member states always underestimate the experimental values slightly. One of the reason of this deviation may be the pairing correlation which may not be included sufficiently in the present calculation, because it will act most strongly in the ground state. Of course, the insufficiency of the deformed-basis AMD wave function and/or the insufficiency of the Gogny D1S force to describe this band would be other reasons, since the excitation energy of the 12^+ state is too low to be explained by only the underestimation of the pairing correlation. Nevertheless we can appreciate the description of the ground band by the present model. The intra-band $E2$ transition probabilities of the ground band are reproduced well without any effective charge (table I). It is to be noted that the calculated excitation energies show a similar characteristic behavior to the experimental values. Namely, in the low-spin states they have a rotational spectrum, but the 10^+ and 12^+ states show the diminish of the excitation energy. This change of the spectrum is closely related to the $\alpha+^{40}\text{Ca}$ clustering in the ground band and will be discussed together with its parity doublet partner, $K^\pi=0_2^-$ band in the next subsection.

Table I. Observed (EXP)²⁶⁾⁻²⁸⁾ and calculated (AMD) intra-band $E2$ transition probabilities $B(E2; J_i^\pi \rightarrow J_f^\pi)$ [e^2fm^4] within the ground band. For the comparison, $\alpha+^{40}\text{Ca}$ RGM (RGM)⁷⁾ and $\alpha+^{40}\text{Ca}(I^\pi)$ OCM (OCM)⁵⁾ results are also shown.

| $J_i^\pi \rightarrow J_f^\pi$ | EXP | RGM | OCM | AMD |
|-------------------------------|--------------|-----|-----|-----|
| $2_1^+ \rightarrow 0_1^+$ | 120 ± 30 | 107 | 166 | 142 |
| $4_1^+ \rightarrow 2_1^+$ | 280 ± 60 | 146 | 231 | 222 |
| $6_1^+ \rightarrow 4_1^+$ | 160 ± 30 | 140 | 212 | 167 |
| $8_1^+ \rightarrow 6_1^+$ | $14 >$ | 118 | 185 | 172 |
| $10_1^+ \rightarrow 8_1^+$ | 140 ± 30 | 75 | 138 | 99 |
| $12_1^+ \rightarrow 10_1^+$ | 40 ± 8 | 34 | 73 | 69 |

4.1.2. $K^\pi=3_1^-$ and 0_1^- bands

The $1\hbar\omega$ excitation from the ground band produces the $K^\pi=0_1^-$ and $K^\pi=3_1^-$ bands in the negative-parity. Though they have different K quanta, these two bands are obtained from the same intrinsic wave function. This induces the rather strong mixing between the $K^\pi=0_1^-$ band members and the natural parity band members of the $K^\pi=3_1^-$ band, and this

mixing enhances the even-odd staggering in the $K^\pi=3_1^-$ band. The obtained $K^\pi=3_1^-$ band corresponds to the experimental $K^\pi=3_1^-$ band which is observed from the 3^- state at 3.17 MeV to the 13^- state at 11.55 MeV. The $1\hbar\omega$ nature of this band is consistent with the results of the shell model calculation.¹¹⁾ We have assigned the calculated $K^\pi=0_1^-$ band members to the observed 1^- (3.76 MeV), 3^- (3.94 MeV) and 5^- (5.21 MeV or 5.31 MeV) states. In the present calculation, member states of this band are obtained up to 9^- state. Though this band is not sufficiently confirmed in experiments, the agreement between the calculation and the experiment seems to be satisfactory at least in the excitation energy.

4.1.3. $K^\pi=0_2^+$ and 2^+ superdeformed bands

In contrast to the $1\hbar\omega$ single-particle excitation in the lowest negative-parity bands, the reconstruction of the mean-field occurs in the positive-parity. The first excited band in the positive-parity states is the $K^\pi=0_2^+$ band which mainly consists of the $4\hbar\omega$ structure. As is discussed in the previous section, this $4\hbar\omega$ structure has a triaxially deformed intrinsic wave function in which four nucleon are excited to the pf -shell from the ^{40}Ca core. Due to this many-particle excitation, the system has a quite different shape of the mean-field and is stabilized by the formation of the elongated superdeformed structure. After the angular momentum projection and the GCM calculation, the excitation energy of this band becomes quite small. It starts from the 0_2^+ state at 1.75 MeV and reaches the 10^+ state at 12.1 MeV in the present calculation. The obtained excitation energies show good agreement with experiments in low-spin states. As the angular momentum increases, the observed spectrum deviates from the rotational one, while the calculated spectrum shows the rotational character. This may be because of the absence of the $2\hbar\omega$ structure in our calculation. In the shell model calculation,¹¹⁾ it is shown that the $2\hbar\omega$ structure becomes dominant as the angular momentum increases in this band and the excitation energies of 10_2^+ and 12_2^+ states are much lower than those expected from the rotational spectrum. In our calculation, we have superposed the wave functions on the energy curve and the $2\hbar\omega$ structure has not appeared on the energy curve. Of course, the obtained wave function in the present calculation is not of the pure $0\hbar\omega$ and $4\hbar\omega$ structure, but also contains $2\hbar\omega$ structure to some extent. However the description of the $2\hbar\omega$ structure seems to be not sufficient in the present calculation. This may also explain the absence of the 12_2^+ state in our calculation.

Since the $4\hbar\omega$ structure has a triaxially deformed intrinsic wave function, $K^\pi=2^+$ band adjoins $K^\pi=0_2^+$ band. The member states of this band are obtained from the 2_3^+ state (3.2 MeV) up to 10^+ (11.3 MeV) state. In the experiment, the possible existence of the low-lying $K^\pi=2^+$ band which starts from the 2^+ state at 2.89 MeV has been long known, and more recently the 8^+ , 10^+ and 12^+ states which possibly belong to this band have been observed

r7.5cm

Table II. Observed (EXP)²⁶⁾⁻²⁸⁾ and calculated (AMD) intra- and inter-band $E2$ transition probabilities $B(E2; J_i^\pi \rightarrow J_f^\pi)$ [$e^2\text{fm}^4$] within the $K^\pi=0_2^+$ and $K^\pi=2^+$ bands. For the comparison, $\alpha+^{40}\text{Ca}(I^\pi)$ coupled-channel OCM (OCM)⁵⁾ results are also shown.

| $K^\pi=0_2^+ \rightarrow K^\pi=0_2^+$ | EXP | OCM | AMD |
|---------------------------------------|--------------------|------|-----|
| $2_2^+ \rightarrow 0_2^+$ | 220 ± 50 | 157 | 320 |
| $4_2^+ \rightarrow 2_2^+$ | 268 ± 50 | 268 | 361 |
| $K^\pi=2^+ \rightarrow K^\pi=2^+$ | EXP | OCM | AMD |
| $3_3^+ \rightarrow 2_3^+$ | < 590 | 185 | 298 |
| $4_3^+ \rightarrow 2_3^+$ | 175_{-60}^{+100} | 148 | 220 |
| $4_3^+ \rightarrow 3_1^+$ | $< 785 \pm 650$ | 11 | 302 |
| $K^\pi=2^+ \rightarrow K^\pi=0_2^+$ | EXP | OCM | AMD |
| $2_3^+ \rightarrow 0_2^+$ | $43 <$ | 3.04 | 24 |

together with their γ transitions to the $K^\pi=0_2^+$ band, though the spin-parity of the (3^+) state is not fixed and the 5^+ , 6^+ , 7^+ , 9^+ and 11^+ states have not been observed yet. The obtained $K^\pi=2^+$ band corresponds to this $K^\pi=2_1^+$ side band. The calculated inter- and intra- $B(E2)$ values within $K^\pi=0_2^+$ and $K^\pi=2_1^+$ bands (table II) are larger than the experimental values, but show similar trend qualitatively.

We note that these two band were also obtained up to 4^+ states by a semi-microscopic cluster model⁵⁾ assuming the $\alpha+^{40}\text{Ca}(0_2^+)$ and $\alpha+^{40}\text{Ca}(2_1^+)$ cluster structure. This result also supports the $4\hbar\omega$ structure of these bands and means the same origin of the $K^\pi=0_2^+$ and $K^\pi=2^+$ bands, since both $^{40}\text{Ca}(0_2^+)$ and $^{40}\text{Ca}(2_1^+)$ states are regarded as having the $\alpha+^{36}\text{Ar}$ cluster structure in their calculation. We also note that their results implies that the $K^\pi=0_2^+$ and $K^\pi=2^+$ bands are possibly regarded as having the $2\alpha+^{36}\text{Ar}$ cluster structure. However, in the case of our AMD result the relation between the superdeformed state and the $2\alpha+^{36}\text{Ar}$ structure is unclear. Indeed, in our calculation this state has a quite large contribution from the spin-orbit force (about -27 MeV in the case of the 0_2^+ state) which is much larger than that expected in the case of the $2\alpha+^{36}\text{Ar}$ structure (about -14 MeV in our calculation).

4.1.4. Hyperdeformation and $^{16}\text{O}+^{28}\text{Si}$ molecular structure

About 19 MeV above the ground state, we have obtained the $K^\pi=0^+$ band which will corresponds to the f^8g^4 state obtained in the Hartree-Fock calculation¹⁵⁾ with large deformation $\beta\sim 0.7$ and it can be classified as a hyperdeformed state. However, as was shown in the previous section, this state has an $^{16}\text{O}+^{28}\text{Si}$ intrinsic structure and it implies that it will be more suitable to understand this state as the $^{16}\text{O}+^{28}\text{Si}$ molecular structure than

to regard as the hyperdeformed state. Indeed this band has its counterpart in the negative parity, $K^\pi=0^-$ band which also has an $^{16}\text{O}+^{28}\text{Si}$ intrinsic wave function. It may be possible to regard these two bands as the parity doublet bands. These bands can have something to do with the possible existence of the $^{16}\text{O}+^{28}\text{Si}$ resonant states.

4.2. $\alpha+^{40}\text{Ca}$ cluster structure

In the previous subsection, we have shown that many kinds of the nuclear excitation appear in the ^{44}Ti and their description by the present model shows satisfactory agreement with experiments. Besides these structures, the existence of the $\alpha+^{40}\text{Ca}$ cluster structure in ^{44}Ti has long been discussed by many authors. In particular, the semi-microscopic cluster model which uses the $\alpha+^{40}\text{Ca}$ optical potential and the $\alpha+^{40}\text{Ca}$ resonating group method calculations^{3),4),7)} have shown the $\alpha+^{40}\text{Ca}$ nature of the ground band and the existence of the excited $N=13, 14$ and 15 bands of the $\alpha+^{40}\text{Ca}$ structure negative-parity. Here N denotes the principal quantum number of the relative motion between α and ^{40}Ca , and is defined as $N=2n + L$ with n and L denoting the number of nodes and the angular momentum of the α -Ca relative wave function, respectively. $N=12$ is the lowest Pauli allowed state which corresponds to the ground state. In this section, we discuss the $\alpha+^{40}\text{Ca}$ clustering in the obtained states on the basis of the microscopic model, deformed-basis AMD, which can also reproduce the excitation mechanism other than the clustering. To clarify our argument, we show the results of two GCM calculations which are obtained by superposing the $0\hbar\omega$ wave functions and $\alpha+^{40}\text{Ca}$ wave functions on the energy curves in Fig. 1 and 3 ($0\hbar\omega+(\alpha+^{40}\text{Ca})$ GCM) and by superposing all of the obtained wave functions (full GCM). The result of the $0\hbar\omega+(\alpha+^{40}\text{Ca})$ GCM shows the existence of the non-small $\alpha+^{40}\text{Ca}$ component in the ground band and the $1\hbar\omega, 2\hbar\omega$ and $3\hbar\omega$ excitation of the relative motion between α and ^{40}Ca in the $N=13, 14$ and 15 bands. The comparison with experiments should be made by the full GCM calculation. We will see that, due to the strong mixing with the $3\hbar\omega$ structure which does not have the $\alpha+^{40}\text{Ca}$ component, $N=13$ and 15 bands are fragmented into several states in the full GCM calculation.

4.2.1. $\alpha+^{40}\text{Ca}$ component in the ground band

In the present calculation, the ground band is the only candidate of the lowest $\alpha+^{40}\text{Ca}$ band among the obtained $K^\pi=0^+$ bands, since other obtained $K^\pi=0^+$ bands have $2\hbar\omega$ or $4\hbar\omega$ excited structure of the ^{40}Ca core. We found that the ground band member states have non-small amounts of the $\alpha+^{40}\text{Ca}$ component except 10_1^+ and 12_1^+ states. The method of the evaluation of the $\alpha+^{40}\text{Ca}$ component in the AMD wave function is explained in the appendix. In the case of the ground state obtained by the full GCM calculation, it amounts to about 39% (table III). However, it is not so large as in the case of the $\alpha+^{16}\text{O}$ component in the

ground state of ^{20}Ne ,²⁾ in which it amounts to about 70%. As is stated in the introduction, due to the increasing core mass and the strong effect of the spin-orbit force, we cannot expect the prominent $\alpha+^{40}\text{Ca}$ cluster structure in the ground band, which is different from the cases of the *sd*-shell nuclei such as ^{16}O and ^{20}Ne . Indeed, the spin-orbit force has a non-small expectation value (-9.5 MeV in the case of the ground state) which must be zero in the case of the $\alpha+^{40}\text{Ca}$ structure. Therefore, we can conclude that the $\alpha+^{40}\text{Ca}$ cluster structure is considerably distorted by the formation of the deformed mean-field and the strong effect of the spin-orbit force.

To understand the distortion of the $\alpha+^{40}\text{Ca}$ cluster structure in the ground band, we first decompose the wave function of the ground state obtained by the full GCM calculation into the $\alpha+^{40}\text{Ca}$ cluster component and other components orthogonal to it. Then we decompose the $\alpha+^{40}\text{Ca}$ cluster component into the SU_3 irreducible representations. The definitions and explanations of this decomposition are presented in the appendix. Similarly to the ground state of the ^{20}Ne , the ground state of ^{44}Ti contains the highly excited $(N, 0)$ components (figure 7). For example, $(N_{min}+8, 0)=(20, 0)$ component which corresponds to the $8\hbar\omega$ excitation in the spherical harmonic oscillator basis still amounts to about 3%. This coherent contribution from $(N, 0)$ states is specific to the cluster correlation. However, we must note that the magnitude of these contribution is quite small compared to the ^{20}Ne . In particular, the contribution from the lowest Pauli-allowed state, $((12, 0)$ state in the case of the ^{44}Ti and $(8, 0)$ state in the case of the ^{20}Ne) is greatly diminished in the ^{44}Ti . This means that the cluster structure is considerably dissolved inside the nucleus, since smaller N means the smaller inter-cluster distance. And the residual coherent contribution from higher $(N, 0)$ components means that the $\alpha+^{40}\text{Ca}$ clustering survives in the surface region, but its contribution is not so large as in ^{20}Ne . In other words, the binding mechanism of the ground band of ^{44}Ti may be rather dominated by the mean-field picture and the $\alpha+^{40}\text{Ca}$ cluster correlation shows up more clearly in the surface region of the nucleus. It is to be noted that the ground band still has a considerable amount of the α spectroscopic factor S_α . Since the smaller $(N, 0)$ components less contributes to the S_α due to the smallness of the μ_N (see Eq.(A.9) in the appendix), the dissolution of the $\alpha+^{40}\text{Ca}$ component in the smaller distance (smaller $(N, 0)$ components) does not affect so much to the S_α . The dominance of the mean-field-like component becomes more prominent as the angular momentum increases. In particular, the 10_1^+ and 12_1^+ states has quite small amount of $\alpha+^{40}\text{Ca}$ components. Instead, in these states, the intrinsic wave functions has an oblately deformed shape. This structure change along the yrast line causes the irregular behavior of the excitation energies of 10_1^+ and 12_1^+ states. The change of the deformation to the oblate shape near the band terminal is due to the nucleon spin alignment to the rotation axis and was also observed in the AMD

calculation of the ^{20}Ne ground band.²⁹⁾

4.2.2. $K^\pi=0_2^-$ band with $\alpha+^{40}\text{Ca}$ structure

It must be noted that the considerable distortion of the $\alpha+^{40}\text{Ca}$ cluster structure in the ground band does not mean the less importance of the $\alpha+^{40}\text{Ca}$ clustering in this nucleus. In the previous section, we have shown that the $1\hbar\omega$ single-particle excitation from the ground state produces the $K^\pi=3_1^-$ and $K^\pi=0_1^-$ bands. From these state, the single-particle excitation is regarded as the one of the basic degrees of the freedom of the excitation in this nucleus. In the same sense, the $\alpha+^{40}\text{Ca}$ clustering is also regarded as one of the basic degrees of freedom of the excitation, since the $K^\pi=0^-$ band in which the system has a considerable amount of the $\alpha+^{40}\text{Ca}$ component is obtained in the present microscopic model calculation. As is shown in the previous section, the wave function on the energy curve which forms the local minimum around $\beta=0.35$ shows a existence of the $\alpha+^{40}\text{Ca}$ clustering in this state. Indeed, when we perform the $0\hbar\omega+(\alpha+^{40}\text{Ca})$ GCM calculation, it produces the $K^\pi=0^-$ band

Table III. Amount of the $\alpha+^{40}\text{Ca}$ component W_J and α spectroscopic factor S_α of the obtained states (see text and appendix). The full GCM results of N=13 and 15 band members and the experimental value of N=13 band members show the sum of the fragmented states.

| ground | $0\hbar\omega+(\alpha+^{40}\text{Ca})$ GCM | | | full GCM | | Exp | N=14 | $0\hbar\omega+(\alpha+^{40}\text{Ca})$ GCM | | | full GCM | |
|-----------------|--|------------|--|----------|------------|------|-----------------|--|------------|--|----------|------------|
| | W_J | S_α | | W_J | S_α | | | W_J | S_α | | W_J | S_α |
| 0 ⁺ | 0.40 | 0.14 | | 0.39 | 0.14 | 0.20 | 0 ⁺ | 0.48 | 0.22 | | 0.46 | 0.22 |
| 2 ⁺ | 0.36 | 0.14 | | 0.34 | 0.12 | 0.20 | 2 ⁺ | 0.43 | 0.23 | | 0.42 | 0.23 |
| 4 ⁺ | 0.33 | 0.14 | | 0.32 | 0.12 | 0.18 | 4 ⁺ | 0.38 | 0.19 | | 0.38 | 0.19 |
| 6 ⁺ | 0.25 | 0.14 | | 0.25 | 0.09 | 0.16 | 6 ⁺ | 0.32 | 0.17 | | 0.30 | 0.17 |
| 8 ⁺ | 0.21 | 0.13 | | 0.21 | 0.08 | 0.13 | 8 ⁺ | 0.23 | 0.14 | | 0.21 | 0.13 |
| 10 ⁺ | 0.06 | 0.01 | | 0.06 | 0.01 | | 10 ⁺ | 0.14 | 0.08 | | 0.12 | 0.08 |
| 12 ⁺ | 0.05 | 0.00 | | 0.06 | 0.00 | | | | | | | |
| N=13 | $0\hbar\omega+(\alpha+^{40}\text{Ca})$ GCM | | | full GCM | | Exp | N=15 | $0\hbar\omega+(\alpha+^{40}\text{Ca})$ GCM | | | full GCM | |
| | W_J | S_α | | W_J | S_α | | | W_J | S_α | | W_J | S_α |
| 1 ⁻ | 0.52 | 0.18 | | 0.56 | 0.20 | 0.25 | 1 ⁻ | 0.63 | 0.34 | | 0.63 | 0.34 |
| 3 ⁻ | 0.48 | 0.16 | | 0.50 | 0.18 | 0.37 | 3 ⁻ | 0.56 | 0.31 | | 0.59 | 0.32 |
| 5 ⁻ | 0.41 | 0.14 | | 0.43 | 0.16 | 0.30 | 5 ⁻ | 0.54 | 0.31 | | 0.56 | 0.31 |
| 7 ⁻ | 0.30 | 0.10 | | 0.38 | 0.12 | | 7 ⁻ | 0.40 | 0.26 | | 0.48 | 0.28 |
| 9 ⁻ | 0.28 | 0.09 | | 0.32 | 0.10 | | 9 ⁻ | 0.30 | 0.18 | | 0.35 | 0.20 |

($N=13$ band) which starts from the 1^- state at 8.9 MeV and the member states of this band have considerable amount of the $\alpha+^{40}\text{Ca}$ component (table III). In the case of the 1^- state, it amounts to about 60%. This band lies in the same energy region as the experimentally observed states. The decomposition of the relative wave function between α and ^{40}Ca shows the growth of the $\alpha+^{40}\text{Ca}$ clustering in this band. Compared to the ground band, the amount of the lowest component ((12,0) in the case of the ground band and (13,0) in the case of the $K^\pi=0_2^-$ band) considerably increases together with the coherent contribution from the higher ($N, 0$) states and they lead to the increase of the S_α in this band (table III). We can say that since the ground state contains the non-small amount of the $\alpha+^{40}\text{Ca}$ component by about 40%, the nucleus exploits this degrees of the freedom in the nuclear excitation. However, when we perform the full GCM calculation, the member states of this band are fragmented into several states because of rather strong mixing with $3\hbar\omega$ structure which does not have $\alpha+^{40}\text{Ca}$ component. In figure 6, the excitation energies of these fragmented states and their averaged energies are plotted. The present model space is not large enough to be directly compared with the observed fragmented states. But, at least, we may be able to say that one of the origin of the observed fragmentation is the mixing of the $\alpha+^{40}\text{Ca}$ structure with the $3\hbar\omega$ non α -clustering structure.

4.2.3. Excited $K^\pi=0^\pm$ bands with $\alpha+^{40}\text{Ca}$ structure

The $\alpha+^{40}\text{Ca}$ clustering as a degree of freedom of the nuclear excitation is reinforced by the existence of the excited state in which the relative inter-cluster motion is excited and have the principal quantum numbers $N=14$ and 15. When we perform the $0\hbar\omega+(\alpha+^{40}\text{Ca})$ GCM, we obtain additional two rotational bands in positive- and negative-parities. These two bands starts from 0_3^+ state at 15.1 MeV and 1_3^- state at 16.9 MeV, respectively, and they contain considerable amount of the $\alpha+^{40}\text{Ca}$ component. We confirmed that these two bands corresponds to $N=14$ and 15 bands by investigating the relative motion (figure 7). Namely, $N=14$ band has a dominant (14,0) component and $N=15$ band has a dominant (15,0) component. The $N=15$ band has a largest amount of the $\alpha+^{40}\text{Ca}$ component among $N=12,13,14$ and 15 bands. This is because of the largest inter-cluster distance of this band which is due to the $4\hbar\omega$ excitation of the relative motion.

When we perform the full GCM calculation, the $N=15$ band members also couple with $3\hbar\omega$ structure and are fragmented. But the energy centroids (averaged energy) are not so different as the excitation energies of the non-fragmented states obtained by the $0\hbar\omega+(\alpha+^{40}\text{Ca})$ GCM. The $N=14$ band has not been fragmented in the present calculation, though its fragmentation is observed in the experiment. We consider that this is due to the absence of the $2\hbar\omega$ structure in our calculation. As is already mentioned, the $2\hbar\omega$ structure does not

appear on the obtained energy curve. And we guess that $2\hbar\omega$ structure is most likely to be coupled with the $N=14$ band, since their principal quantum numbers are equal.

§5. Summary

We have studied the low-lying level structure of ^{44}Ti by using the framework of the deformed-basis AMD with the Gogny D1S force. We have shown that many kinds of mutually very different nuclear excitation appearing in this nucleus are very well reproduced unifiedly in a single AMD framework. Namely, the single-particle excitation in the $K^\pi=3_1^-$ and $K^\pi=0_1^-$ bands, the formation of the triaxial superdeformed states in the $K^\pi=0_2^+$ and $K^\pi=2^+$ bands, and the $\alpha+^{40}\text{Ca}$ clustering in some $K^\pi=0^\pm$ bands. The possible existence of the $^{16}\text{O}+^{28}\text{Si}$ molecule-like structure is also suggested in the present calculation. The triaxial superdeformed state suggested by some Hartree-Fock calculations are confirmed and it has been shown that this superdeformed state explains the low-lying $K^\pi=0_2^+$ and 2^+ bands, which suggests the interpretation of the low-lying states of these bands as the triaxial rotor. Among these state, we have focused on the $\alpha+^{40}\text{Ca}$ clustering in the low-energy region. We found that the $\alpha+^{40}\text{Ca}$ cluster component in the ground band is considerably dissolved by the formation of the deformed mean-field and the spin-orbit force. But, since the ground state still contains non-small amount of the $\alpha+^{40}\text{Ca}$ component by about 40%, it is possible to excite the nucleus by using the clustering as a degree of the freedom of nuclear excitation. This excitation leads to the existence of the $K^\pi=0^\pm$ bands in which the relative motion between α and ^{40}Ca have the principal quantum number $N=13, 14$ and 15 . However, due to the coupling to $3\hbar\omega$ structures, $N=13$ and 15 bands members are fragmented into several states. When we average their energies for each spin, these bands lie in the same energy region of the observed $\alpha+^{40}\text{Ca}$ bands with $N=13, 14$ and 15 .

Acknowledgements

We would like to thank Dr. Y. Kanada-En'yo for valuable discussions. Many of the computational calculations were carried out by SX-5 at Research Center for Nuclear Physics, Osaka University (RCNP). This work was partially performed in the Research Project for Study of Unstable Nuclei from Nuclear Cluster Aspects sponsored by Institute of Physical and Chemical Research (RIKEN).

Appendix

The definition and the explanation of the $\alpha+^{40}\text{Ca}$ component in the AMD wave function and its decomposition into the SU_3 irreducible representations are presented. The reader is directed to references^{30),31)} for more details.

A.1. $\alpha+^{40}\text{Ca}$ component in the AMD wave function

The $\alpha+^{40}\text{Ca}$ system is generally expressed by the RGM-type wave function.

$$\Phi_{\alpha+^{40}\text{Ca}}^{J\pi} = n_0 \mathcal{A}\{\chi_J(r) Y_{J0}(\hat{r}) \phi(\alpha) \phi(^{40}\text{Ca})\}, \quad (\text{A.1})$$

$$n_0 = \sqrt{40! \cdot 4! / 44!}, \quad \pi = (-)^J. \quad (\text{A.2})$$

Here, \mathcal{A} is the antisymmetrizer, \mathbf{r} is the relative coordinate between α and ^{40}Ca , $\phi(\alpha)$ and $\phi(^{40}\text{Ca})$ are the normalized internal wave function of the clusters. $\chi_J(r)$ is the radial wave function of the relative motion between α and ^{40}Ca , and is so normalized that $\Phi_{\alpha+^{40}\text{Ca}}^J$ is normalized to unity.

The normalized deformed-base AMD+GCM wave function $\Phi_M^{J\pi}$ of ^{40}Ca is divided into the $\alpha+^{40}\text{Ca}$ component and the residual part $\Phi_R^{J\pi}$.

$$\Phi_M^{J\pi} = \alpha \Phi_{\alpha+^{40}\text{Ca}}^{J\pi} + \sqrt{1 - \alpha^2} \Phi_R^{J\pi}. \quad (\text{A.3})$$

$\Phi_R^{J\pi}$ is also normalized and orthogonal to the $\Phi_{\alpha+^{40}\text{Ca}}^{J\pi}$. We introduce the projection operator \mathcal{P}_L which projects out the $\alpha+^{40}\text{Ca}$ component from the $\Phi_M^{J\pi}$,

$$\begin{aligned} \mathcal{P}_L \Phi_M^{J\pi} &= \alpha \Phi_{\alpha+^{40}\text{Ca}}^{J\pi} \\ &= \alpha n_0 \mathcal{A}\{\chi_J(r) Y_{J0}(\hat{r}) \phi(\alpha) \phi(^{40}\text{Ca})\}. \end{aligned} \quad (\text{A.4})$$

The practical formula of \mathcal{P}_L used in this study is given later. Using this projection operator, the squared amplitude of the $\alpha+^{40}\text{Ca}$ component (amount of the $\alpha+^{40}\text{Ca}$ component) W_J of $\Phi_M^{J\pi}$ is written as,

$$W_J = |\alpha|^2 \equiv \langle \Phi_M^{J\pi} | \mathcal{P}_L | \Phi_M^{J\pi} \rangle. \quad (\text{A.5})$$

A.2. Decomposition of the $\alpha+^{40}\text{Ca}$ component into SU_3 irreducible representations

If the internal wave functions $\phi(\alpha)$ and $\phi(^{40}\text{Ca})$ are expressed by the H.O. wave functions with oscillator parameter ν , Eq. (A.1) and (A.4) are easily decomposed into SU_3 irreducible representations. When we expand $\chi_J(r)$ by the radial wave function of the H.O. $R_{NJ}(r, \gamma)$ with $N=2n+J$ and the width parameter $\gamma = \frac{4 \cdot 40}{44} \nu$ as

$$\chi_J(r) = \sum_N e_{NJ} R_{NJ}(r, \gamma), \quad (\text{A.6})$$

the norm of Eq. (A.1) is written as

$$\langle \Phi_{\alpha+^{40}\text{Ca}}^{J\pi} | \Phi_{\alpha+^{40}\text{Ca}}^{J\pi} \rangle = \sum_N \mu_N e_{NJ}^2 = 1, \quad (\text{A}\cdot 7)$$

and therefore, the squared amplitude of the $\alpha+^{40}\text{Ca}$ is rewritten as

$$W_J = |\alpha|^2 = |\alpha|^2 \sum_N \mu_N e_{NJ}^2. \quad (\text{A}\cdot 8)$$

and the α spectroscopic factor S_α is defined as,

$$S_\alpha^J \equiv |\alpha|^2 \sum_N \mu_N^2 e_{NJ}^2. \quad (\text{A}\cdot 9)$$

Here, the eigenvalue of the RGM norm kernel μ_N is defined as

$$\begin{aligned} \mu_N \equiv & \langle R_{NJ}(r) Y_{J0}(\hat{r}) \phi(\alpha) \phi(^{40}\text{Ca}) | \\ & \mathcal{A}\{R_{NJ}(r) Y_{J0}(\hat{r}) \phi(\alpha) \phi(^{40}\text{Ca})\} \rangle, \end{aligned} \quad (\text{A}\cdot 10)$$

and it has a non-zero value for $N \geq 12$ in the case of the $\alpha+^{40}\text{Ca}$ system. The Eq. (A.10) means that the quantity $|\alpha|^2 \mu_N e_{NJ}^2$ is equal to the amount of the $SU_3(N, 0)$ irreducible representations which is contained in $\alpha \Phi_{\alpha+^{40}\text{Ca}}^{J\pi}$, since both $\phi(\alpha)$ and $\phi(^{40}\text{Ca})$ are SU_3 scalar and therefore, the $\alpha+^{40}\text{Ca}$ system which has a relative motion $\chi_J(r) = R_{NJ}(r, \gamma)$ belongs to $SU_3(N, 0)$.

A.3. Approximation of the projection operator \mathcal{P}_L

To evaluate W_J and e_{NJ} , we have approximated the projection operator \mathcal{P}_L by the set of the orthonormalized angular-momentum-projected Brink-type wave functions. We start from the Brink-type wave function $\varphi_B(R_i)$ in which α and ^{40}Ca are located at the points $(0, 0, \frac{40}{44}R_i)$ and $(0, 0, -\frac{4}{44}R_i)$, respectively,

$$\varphi_B(R_i) = n_0 \mathcal{A}\left\{ \varphi\left(\alpha, \frac{40}{44}\mathbf{R}_i\right), \varphi(^{40}\text{Ca}, -\frac{4}{20}\mathbf{R}_i) \right\}, \quad (\text{A}\cdot 11)$$

$$\mathbf{R}_i \equiv (0, 0, R_i). \quad (\text{A}\cdot 12)$$

For simplicity, $\varphi(\alpha)$ and $\varphi(^{40}\text{Ca})$ are described by the AMD wave functions which are obtained by the variational calculation without any constraint potential and with the fixed spherical width parameter $\nu=0.150$. And we have assumed that these wave functions approximate well the SU_3 limits. By separating the center-of-mass wave function $\omega(\mathbf{X}_G)$, the internal wave function $\varphi_C(R_i)$ is written as

$$\varphi_B(R_i) = \omega(\mathbf{X}_G) \varphi_C(R_i), \quad (\text{A}\cdot 13)$$

$$\varphi_C(R_i) = n_0 \mathcal{A} \{ \Gamma(\mathbf{r}, \mathbf{R}_i, \gamma) \phi(\alpha) \phi(^{40}\text{Ca}) \}, \quad (\text{A}\cdot 14)$$

$$\Gamma(\mathbf{r}, \mathbf{R}_i, \gamma) = \left(\frac{2\gamma}{\pi} \right)^{3/4} e^{-\gamma(\mathbf{r}-\mathbf{R}_i)^2}, \quad (\text{A}\cdot 15)$$

$$\omega(\mathbf{X}_G) = \left(\frac{44 \cdot 2\nu}{\pi} \right)^{3/4} \exp(-44\nu \mathbf{X}_G^2), \quad (\text{A}\cdot 16)$$

$$\mathbf{X}_G = \frac{1}{44} \sum_{i=1}^{44} \mathbf{r}_i, \quad \gamma = \frac{40 \cdot 4}{44} \nu, \quad (\text{A}\cdot 17)$$

where $\Gamma(\mathbf{r}, \mathbf{R}_i, \gamma)$ is the relative wave function between α and ^{40}Ca of the Brink-type wave function. The angular-momentum-projected Brink-type wave function $\phi_C^J(R_i)$ is obtained from the $\phi_C(R_i)$,

$$\varphi_C^J(R_i) = q_i^J P_{00}^J \varphi_C(R_i). \quad (\text{A}\cdot 18)$$

P_{00}^J is the angular momentum projector and q_i^J is the normalization factor. The orthonormalized set of the angular-momentum-projected Brink-type wave functions $\tilde{\varphi}_\alpha^J$ is described by the linear combination of the $\varphi_C^J(R_i)$,

$$\tilde{\varphi}_\alpha^J = \frac{1}{\sqrt{\rho_\alpha}} \sum_i c_{i\alpha} \varphi_C^J(R_i), \quad (\text{A}\cdot 19)$$

and the coefficients ρ_α and $c_{i\alpha}$ are the eigenvalues and eigenvectors of the overlap matrix $B_{ij} = \langle \varphi_C^J(R_i) | \varphi_C^J(R_j) \rangle$,

$$\sum_j B_{ij} c_{j\alpha} = \rho_\alpha c_{i\alpha}. \quad (\text{A}\cdot 20)$$

If the number of the basis wave functions $\tilde{\varphi}_\alpha^J$ is taken enough, the projection operator \mathcal{P}_L is approximated by the set of $\tilde{\varphi}_\alpha^J$,

$$\begin{aligned} \mathcal{P}_L &\simeq \sum_\alpha |\tilde{\varphi}_\alpha^J\rangle \langle \tilde{\varphi}_\alpha^J|, \\ &= \sum_{ij} B_{ji}^{-1} |\varphi_C^J(R_i)\rangle \langle \varphi_C^J(R_j)|. \end{aligned} \quad (\text{A}\cdot 21)$$

In the present calculation, we have employed 19 Brink-wave functions in which R_i is taken as $R_i = 1.0, 1.5, 2.0, \dots, 10.0$ fm.

Using Eq. (A·21), Eq. (A·4) and Eq. (A·5) are rewritten as

$$\begin{aligned} \mathcal{P}_L \Phi_M^{J\pi} &= \alpha n_0 \mathcal{A} \{ \chi_J(r) Y_{J0}(\hat{r}) \phi(\alpha) \phi(^{40}\text{Ca}) \}, \\ &\simeq \sum_{ij} B_{ji}^{-1} \langle \varphi_C^J(R_j) | \Phi_M^{J\pi} | \varphi_C^J(R_i) \rangle, \end{aligned} \quad (\text{A}\cdot 22)$$

$$\begin{aligned} |\alpha|^2 &\simeq \sum_{ij} \langle \varphi_C^J(R_j) | \Phi_M^{J\pi} \rangle B_{ji}^{-1} \\ &\quad \times \langle \Phi_M^{J\pi} | \varphi_C^J(R_i) \rangle. \end{aligned} \quad (\text{A}\cdot 23)$$

The expansion coefficient e_N of $\chi_J(r)$ is obtained from Eq. (A·22). We expand wave function of the relative motion $\gamma(\mathbf{r}, \mathbf{R}_i, \gamma)$ of Eq. (A·24),

$$\Gamma(\mathbf{r}, \mathbf{R}_i, \gamma) = e^{-\frac{\gamma}{2}R_i^2} \sum_{NJm} \left\{ \frac{(\gamma R_i^2)^{\frac{N}{2}}}{\sqrt{N!}} \times \sqrt{\frac{4\pi}{2J+1}} A_J^N Y_{Jm}(\hat{R}_i) R_{NJ}(r, \gamma) Y_{Jm}(\hat{r}) \right\}, \quad (\text{A}\cdot 24)$$

$$A_J^N \equiv (-)^{(N-J)/2} \sqrt{\frac{(2J+1) \cdot N!}{(N-J)!! \cdot (N+J+1)!!}}. \quad (\text{A}\cdot 25)$$

And using Eq. (A·14) and (A·24), Eq. (A·18) is rewritten as

$$\varphi_C^J(R_i) = n_0 \mathcal{A} \{ \chi_J^{(i)}(r) Y_{J0}(\hat{r}) \phi(\alpha) \phi(^{40}\text{Ca}) \}, \quad (\text{A}\cdot 26)$$

$$\chi_J^{(i)}(r) = q_i^J e^{-\frac{\gamma}{2}R_i^2} \sum_N \frac{(\gamma R_i^2)^{\frac{N}{2}}}{\sqrt{N!}} A_J^N R_{NJ}(r). \quad (\text{A}\cdot 27)$$

By inserting Eq. (A·26) into Eq. (A·22), we obtain $\chi_J(r)$ as a superposition of $\chi_J^{(i)}(r)$,

$$\chi_J(r) \simeq \frac{1}{\alpha} \sum_{ij} \langle \varphi_C^J(R_j) | \Phi_M^{J\pi} \rangle B_{ji}^{-1} \chi_J^{(i)}(r). \quad (\text{A}\cdot 28)$$

Inserting (A·27) into Eq. (A·28), e_N is given as

$$e_N = \frac{1}{\alpha} A_J^N \sum_{ij} \left\{ \langle \varphi_C^J(R_j) | \Phi_M^{J\pi} \rangle B_{ji}^{-1} \times q_i^J e^{-\frac{\gamma}{2}R_i^2} \frac{(\gamma R_i^2)^{\frac{N}{2}}}{\sqrt{N!}} \right\}. \quad (\text{A}\cdot 29)$$

References

- 1) Y.Fujiwara, H.Horiuchi, K.Ikeda, M.Kamimura, K.Kato, Y.Suzuki and E.Uegaki, Prog. Theor. Phys. Supplement No.68, Chapter II, 29 (1980).
- 2) M. Kimura, Phys. Rev. C (2004),
- 3) H. Kihara, M. Kamimura, and A. Tohsaki-Suzuki, Proc. Int. Conf. on Nuclear Structure, Contributed Papers, Int. Academic Printing, Tokyo, 1977, pp.234, 235.
- 4) A. Arima, Proc. Topical Conf. on Physics of Medium Light Nuclei, Editrice Compositori, Bologna, 1978, p.19.
- 5) F. Michel, S. Ohkubo, and G. Reidemeister, Prog. Theor. Phys. Supplement 132, Chapter II, 7 (1998), and references therein.

- 6) Th. Delbar, Gh. Grégoire, G. Paic, R. Ceuleneer, F. Michel, R. Vanderpoorten, A. Budzanowski, H. Dabrowski, L. Freindl, K. Garotowski, S. Micek, R. Planeta, A. Strzalkowski, and K. A. Eberhard, Phys. Rev. **C 18**, 1237 (1978).
- 7) T. Wada and H. Horiuchi, Phys. Rev. **C 38** 2063 (1988).
- 8) T. Yamaya, K. Katori, M. Fujiwara, S. Kato, and S. Ohkubo, Prog. Theor. Phys. Supplement **132**, Chapter III, 73 (1998), and references therein.
- 9) C. E. Svensson et al., Phys. Rev. Lett. **85**, 2693 (2000).
- 10) E. Ideguchi et al., Phys. Rev. Lett. **87**, 222501 (2001).
- 11) C. D. O'Leary, M. A. Bentley, B. A. Brown, D. E. Appelbe, R. A. Bark, D. M. Cullen, S. Ertürk, A. Maj, and A. C. Merchant, Phys. Rev. **C 61**, 064314 (2000).
- 12) J. J. Simpson, W. R. Dixon, and R. S. Storey, Phys. Rev. Lett. **31**, 946 (1973); J. J. Kolata, J. W. Olness, and E. K. Warburton, Phys. Rev. **C 10**, 1663 (1974).
- 13) A. Arima, V. Gillet, and J. Ginocchio, Phys. Rev. Lett. **25**, 1043 (1970).
- 14) D. C. Zheng, D. Berdichevsky, and L. Zamick, Phys. Rev. **C 38**, 437 (1988).
- 15) T. Inakura, S. Mizutori, M. Yamagami, and K. Matsuyanagi, Nucl. Phys. **A 710**, 261 (2002).
- 16) M. Kimura and H. Horiuchi, submitted to Phys. Rev. C.
- 17) Y. Kanada-En'yo, M. Kimura, and H. Horiuchi, Comptes Rendus Physique **4**, 497 (2003).
- 18) M. Yamagami and K. Matsuyanagi, Nucl. Phys. **A672**, 123 (2000).
- 19) H. Molique, J. Dobaczewski, and J. Dudek, Phys. Rev. **C61**, 044304 (2000).
- 20) R.R.Rodríguez-Guzmán, J.L.Egido and L.M.Robledo, Phys. Rev. **C62**, 054308 (2000).
- 21) S. Ohkubo and K. Yamashita, Phys. Rev. **C 66**, 021301(R) (2002).
- 22) Y. Kondo, B. A. Robson, and R. Smith, Phys. Lett. **B 227**, 310 (1989); J. Phys. Soc. Japan Supple. **58**, 597 (1989).
- 23) M. Kimura and H. Horiuchi, Prog. Theor. Phys. **107**, 33 (2002).
- 24) J. Dechargé and D. Gogny, Phys. Rev. **C 21**, 1568 (1980).
- 25) A. Dote, H. Horiuchi and Y. Kanada-Enyo, Phys. Rev. **C56**, 1844 (1997).
- 26) J. J. Simpson, W. R. Dixon and R. S. Storey, Phys. Rev. Lett **31**, 946 (1973).
- 27) J. J. Simpson, W. R. Dixon and R. S. Storey, Phys. Rev. **C11**, 1828 (1975).
- 28) J. Britz, A. Chevallier, J. Chevallier and B. Haas, Nucl. Phys. **A262**, 189 (1976).
- 29) Y. Kanada-Enyo and H. Horiuchi, Prog. Theor. Phys. **93**, 115 (1995).
- 30) Y. Kanada-En'yo and H. Horiuchi, Phys. Rev. **C68**, 014319 (2003).
- 31) H. Horiuchi, Prog. Theor. Phys. Suppl. **62** Chapter III (1977).

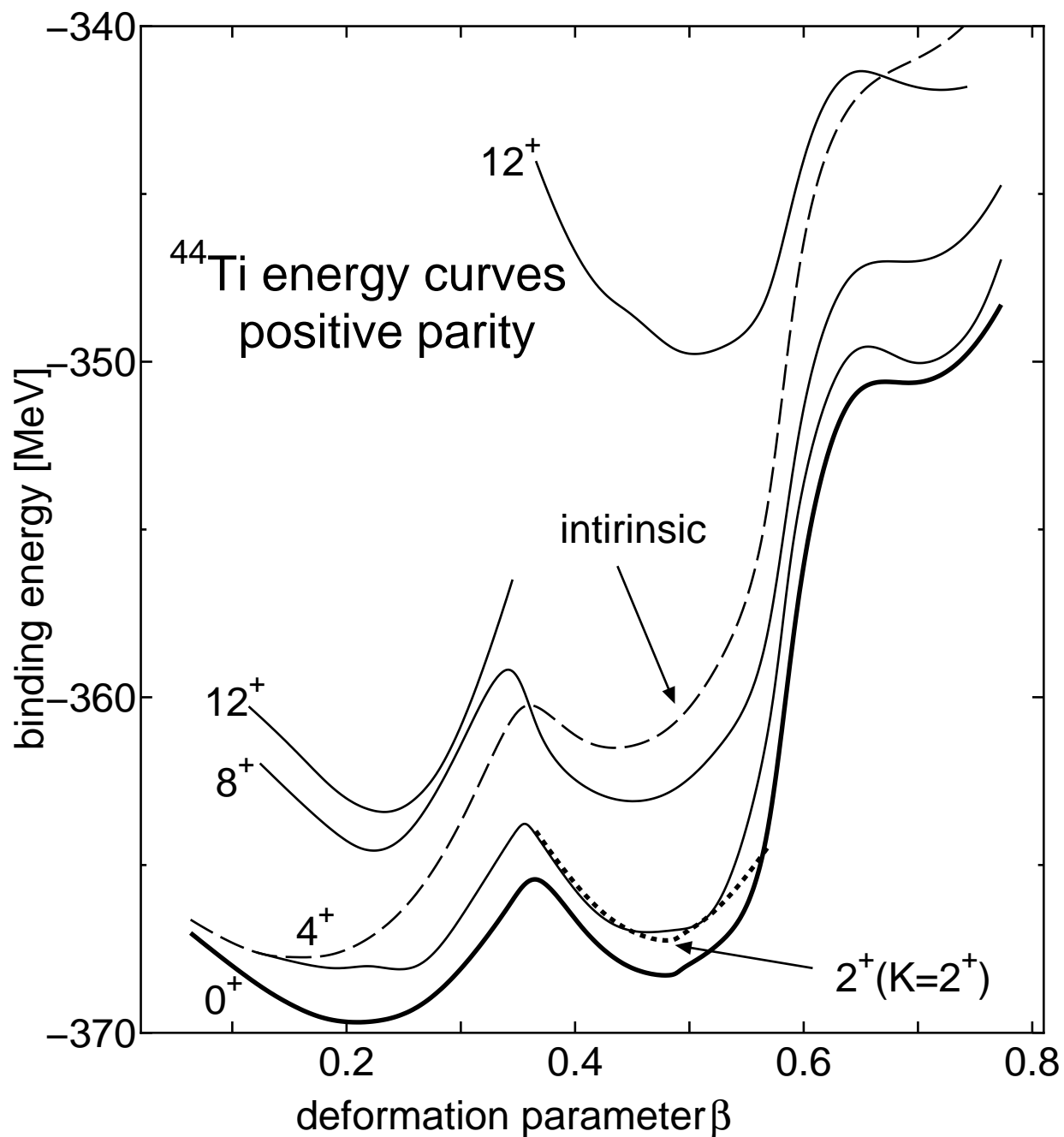


Fig. 1. Energy curves for each spin state as functions of the quadrupole deformation parameter β . 0^+ , 4^+ , 8^+ and 12^+ states are shown for the presentation. The 2^+ state which is the band head state of $K^\pi=2^+$ band is shown by the dotted line. The parity-projected intrinsic state (before the angular momentum projection) is also shown by the dashed line.

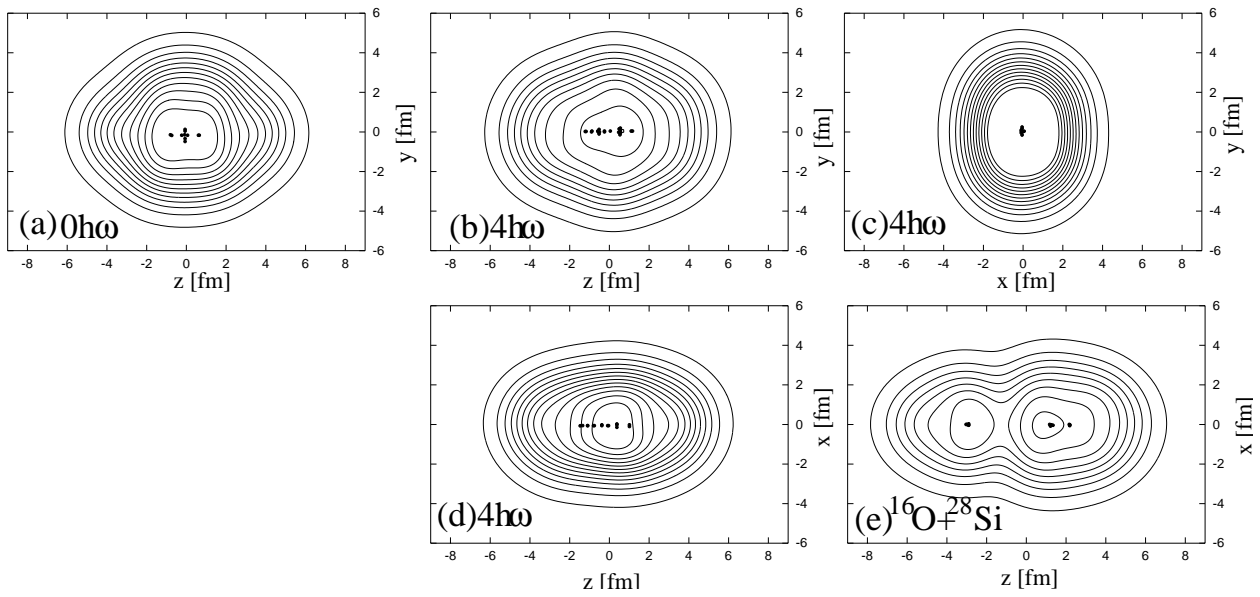


Fig. 2. Density distributions of the intrinsic wave functions obtained by the variational calculation after the projection to positive parity. (a) shows the density distribution for the $0\hbar\omega$ configuration. (b), (c) and (d) show that for the $4\hbar\omega$ configuration plotted from different angles. (e) shows that for the $^{16}\text{O} + ^{28}\text{Si}$ configuration. Black points in these figures show the forty-four centroids of the single particle wave packets ($\mathfrak{R}(\mathbf{Z}_i)$) in the coordinate space.

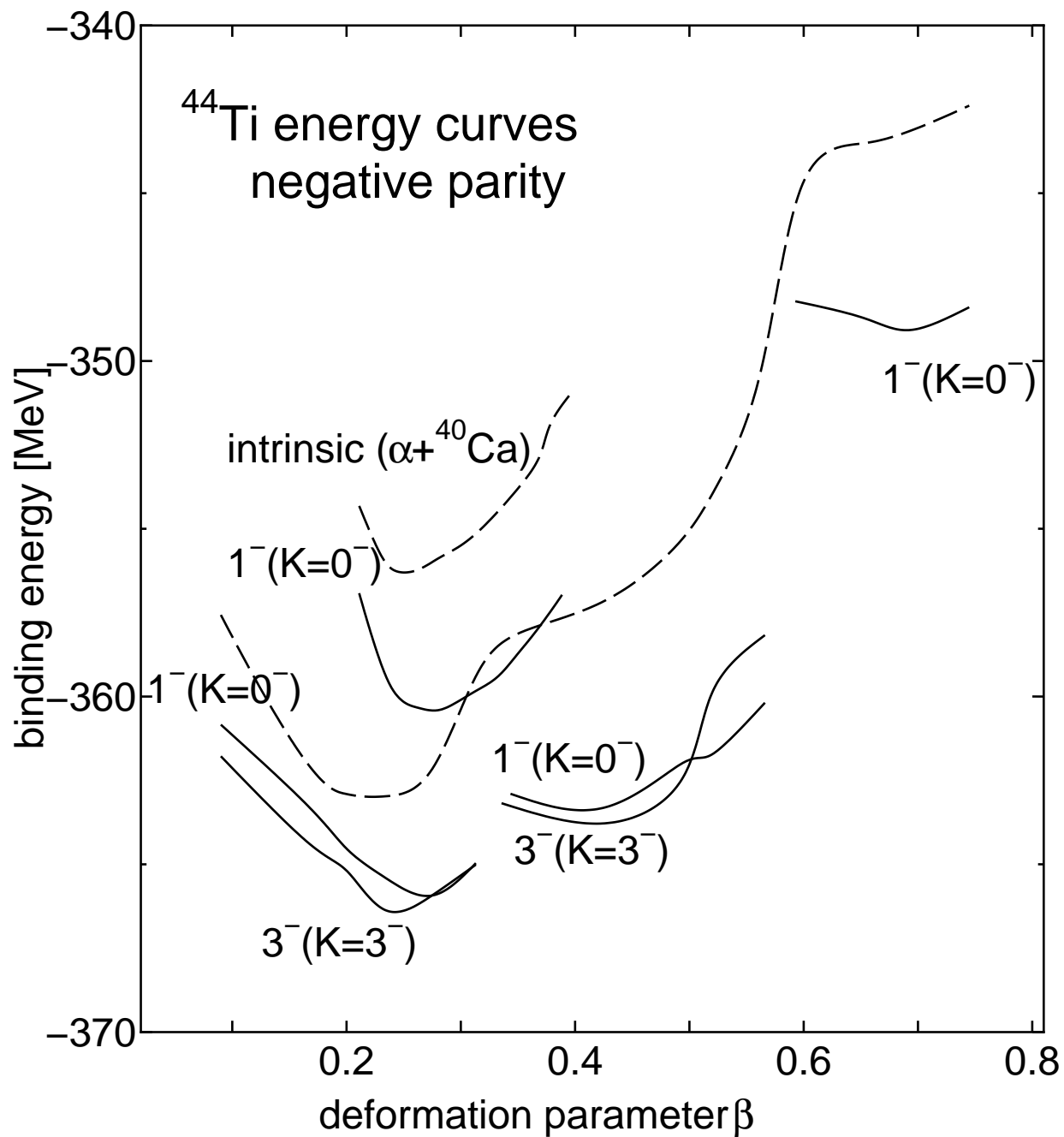


Fig. 3. Energy curves for each spin state as functions of the quadrupole deformation parameter β . Only the band head states are shown for the presentation. The parity-projected intrinsic state (before the angular momentum) is also shown by the dashed line.

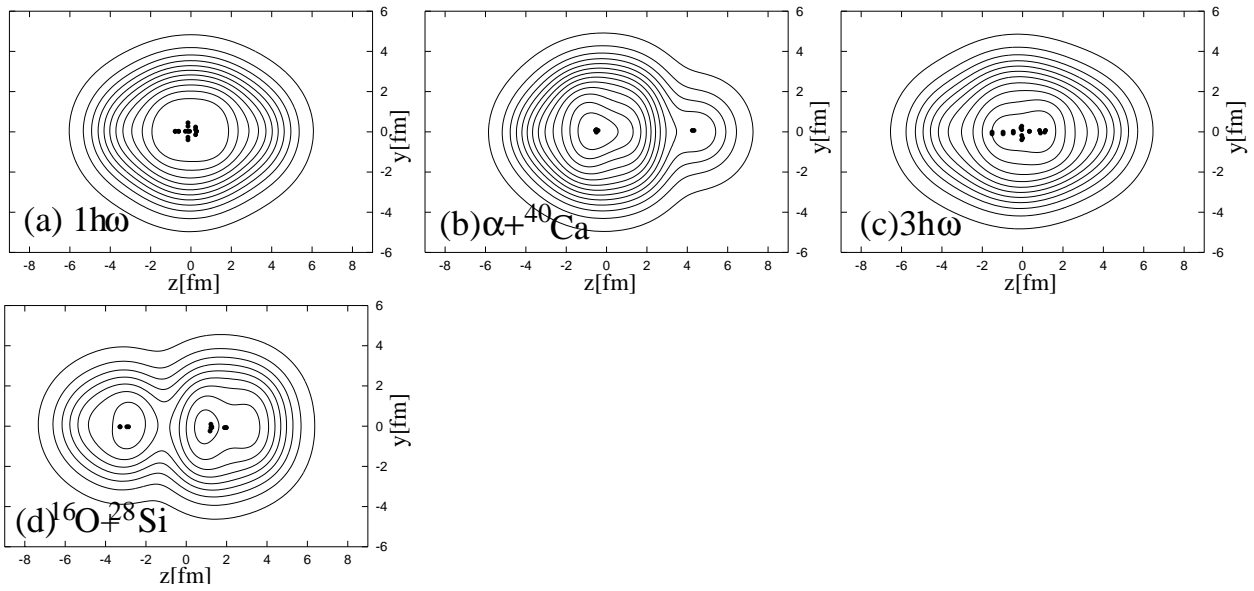


Fig. 4. Density distributions of the intrinsic wave functions obtained by the variational calculation after the projection to negative parity. (a) and (c) shows the density distribution for the $1\hbar\omega$ and $3\hbar\omega$ configurations, respectively. (b) shows that for the $\alpha+^{40}\text{Ca}$ configuration. (d) shows that for the $^{16}\text{O}+^{28}\text{Si}$ configuration. Black points in these figures show the forty-four centroids of the single particle wave packets ($\Re(\mathbf{Z}_i)$) in the coordinate space.

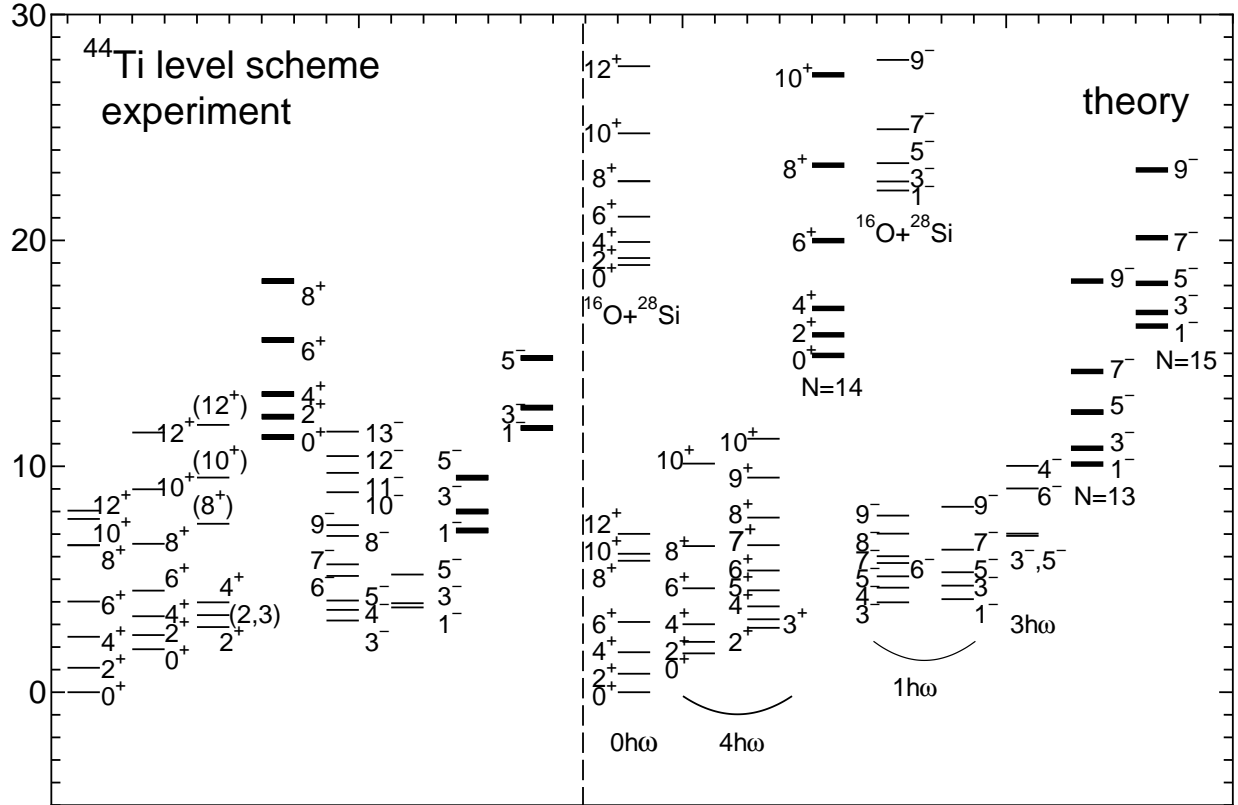


Fig. 5. Observed and calculated level scheme of ^{44}Ti . Only the observed states which correspond to the calculated states are shown. In the calculated results, the main component of each band is shown below the band head state (ex. $0\hbar\omega$) as a guide. The states plotted by the bold lines in both experiment and theory correspond to the $\alpha+^{40}\text{Ca}$ cluster states. These states except of N=14 band in the theoretical result are shown by the averaged energy of the fragmented states (see next subsection).

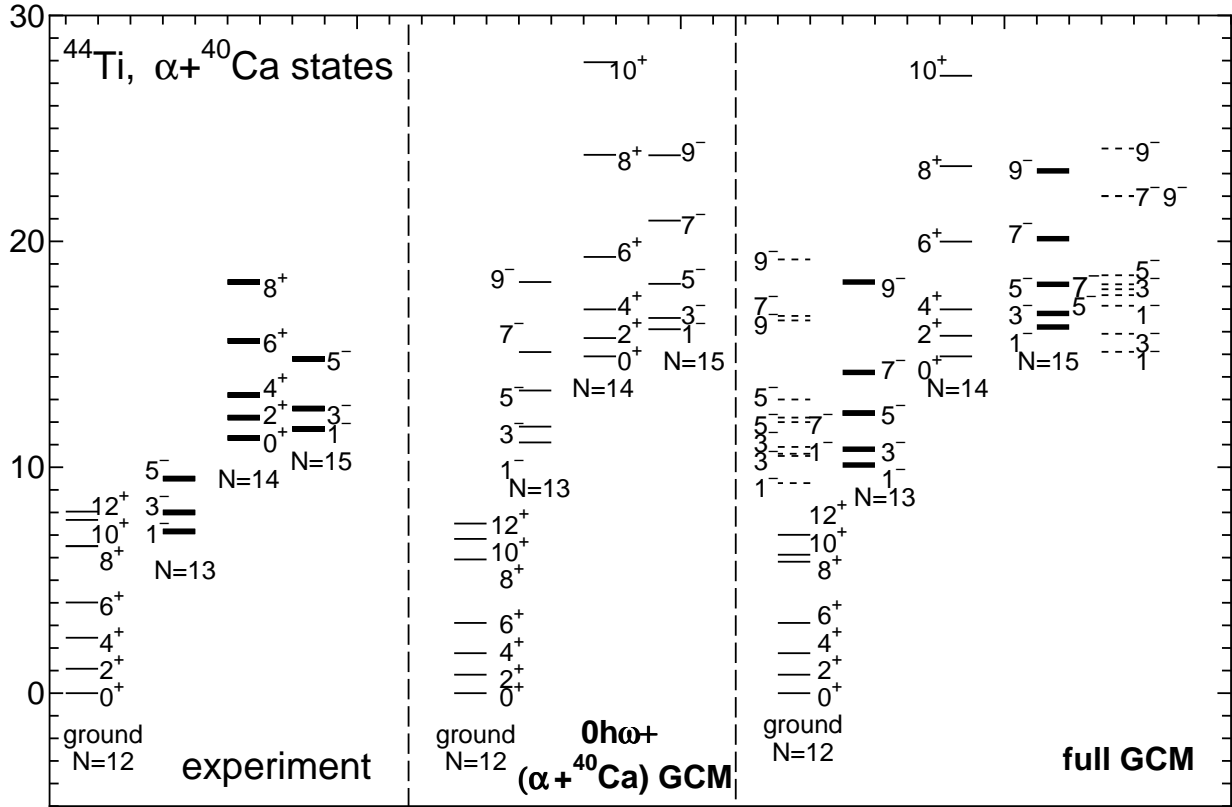


Fig. 6. Observed⁸⁾ and calculated ($0\hbar\omega + (\alpha + ^{40}\text{Ca})$ GCM and full GCM) states of ^{44}Ti which have the $\alpha + ^{40}\text{Ca}$ cluster structure. The bold lines indicate the energy centroid of the experimental ($N=13, 14$ and 15) and theoretical (full GCM, $N=13$ and 15) fragmented states. The dotted lines indicate the energy of the fragmented states obtained by the full GCM calculation.

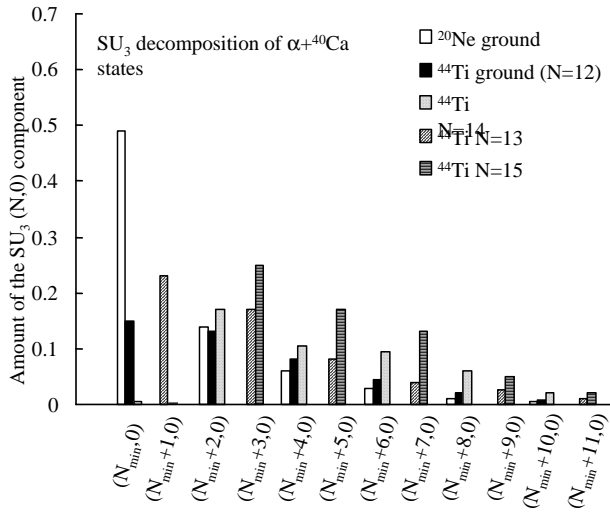


Fig. 7. The decomposition of the $\alpha+^{40}\text{Ca}$ component into the SU_3 irreducible representations. These results are calculated from the $0\hbar\omega+(\alpha+^{40}\text{Ca})$ GCM wave functions. For comparison, the result of the ground band of ^{20}Ne is also shown. N_{min} indicates the lowest Pauli-allowed states. $N_{min}=12$ and $N_{min}=8$ for ^{44}Ti and ^{20}Ne , respectively.